SUPPLEMENTAL INFORMATION

Supplemental Table

	0 stims (Control)	< 5 stims	5 stims	>5 stims
Count	11	13	24	7

Supplemental Table 1 Number of stimulations per session. Related to Figure 1.

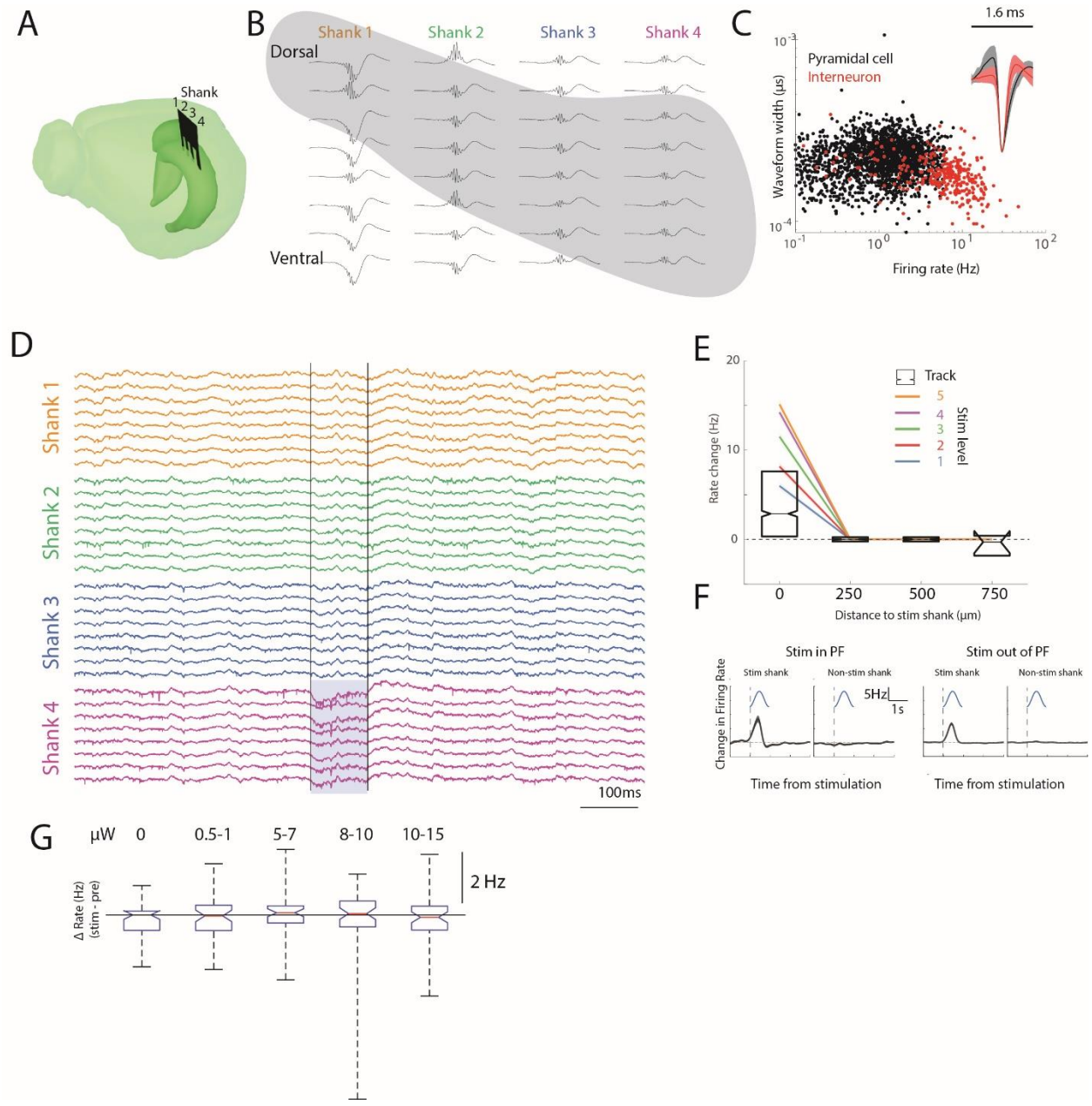

Figure S1. µLED stimulation induces focal neural depolarization in dorsal CA1; related to main Figures 1 and 2. *(A)* A 32 channel, 4 shank µLED probe was implanted at a 45º angle to the midline to record from the longitudinal axis of dorsal CA1. *(B)* Electrode placement was confirmed online through the recording of sharp-wave ripples (SPW-Rs). The mean SPW-R for an example session is plotted, aligned to the ripple trough associated with the highest power in the bandpass filtered LFP (ripple bandpass filter = (140 - 200Hz). Shaded grey region indicates str. pyramidale as estimated from the SPW-R profile. *(C)* Pyramidal cells and interneurons were classified using extracellularly recorded features, including spike width and neural firing rate. *Inset*, mean ± STD waveform of all pyramidal cells and interneurons in the database. *(D)* Example 1 s sweep showing stimulation on shank 4 induced robust spiking only on that stimulated shank. *(E)* While mice were in the homecage, calibration pulses were given to

determine the amount of light to deliver on the track. Five intensities (1-5, colored lines) were chosen in equal steps of light power from the lowest level that reliably induced spiking (as determined through online inspection), to the highest level that did not induce an artificial ripple. The highest intensity used for calibration in the homecage was used to stimulate neurons on the track. The box plot shows the summary statistics across pyramidal cells for the mean firing rate during the peak of the track stimulation (250 – 750 ms into the half-sine pulse). Note the dramatically lower firing rates during track running compared to homecage stimulation despite equal intensity light delivery. *(F)* Optogenetic stimulation increased firing rates of neurons on the stimulated shank, regardless of whether light was delivered within, or outside of, a pre-existing place field. *(G)* No firing rate changes were seen with μLED stimulation in CaMKIIα-GFP mice (lacking ChR2) at light levels used throughout these experiments (N = 2 mice, N = 48 stimulated neurons).

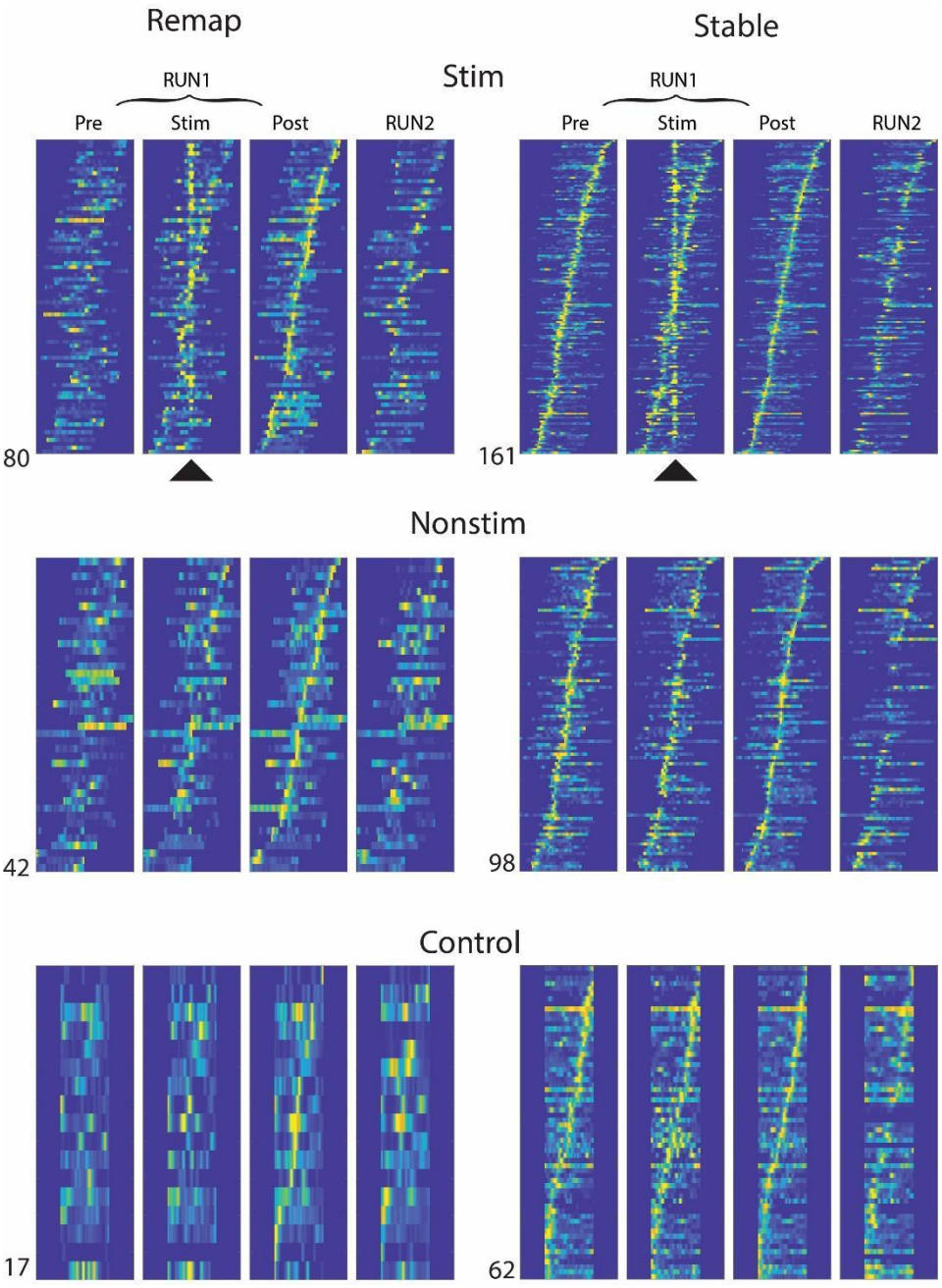

Figure S2. All place fields in the database; related to Figure 2. Place fields are centered on the stimulation location or the center of the track for Control sessions, and plotted using spikes recorded before stimulation (pre), during stimulation trials (stim), directly after stimulation (Post), and during a follow-up track session after homecage recordings (RUN2). Place fields sorted by post-Stim peak firing location. See STAR methods for how neurons were classified as remapping versus stable.

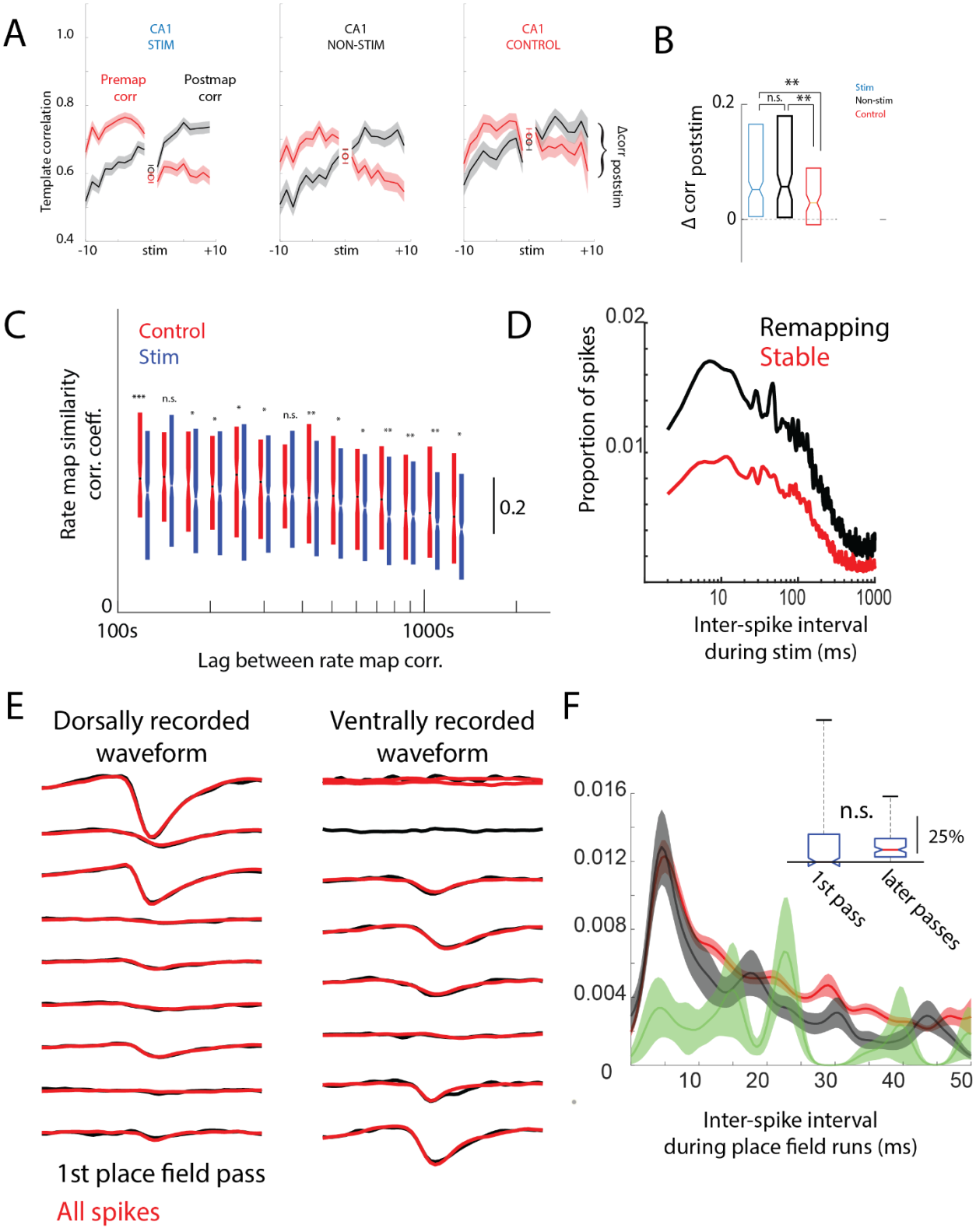

Figure S3. Alternate metric to quantify remapping; related to Figure 3. (A) Correlations of trial-by-trial rate maps against templates defined by pre-stimulation activity (Premap corr) and against post-stimulation activity (Postmap corr). The mean difference between these templates post-

stimulation ($\Delta template_{poststim}$) shows the degree of place field remapping after stimulation. *(B)* Both stimulated ($p = 0.006$) and non-stimulated neurons ($p= 0.002$) showed more place field reorganization than neurons recorded in Control sessions. No difference ($p = 0.3$) was observed between stimulated and non-stimulated neurons during stimulation sessions. *(C)* The rate of place field trial-by-trial decorrelation (drift) was quantified for neurons on the stimulated shank versus Control neurons recorded on sessions where no light was given. In general, place fields decorrelated over time. At long and short intervals between compared place field maps, optogenetic stimulation induced larger rate map decorrelations. * $p < .05$, ** $p < .01$, *** $p < .001$. *(D)* The mean histogram for the inter-spike interval of spikes during stimulation for neurons that remapped (black) versus those that showed stable place fields (red). Significant differences were observed at all intervals and especially at short ISIs, consistent with more bursting during stimulation. *(E)* Waveforms recorded on the first pass through a new place field (black) did not differ from those recorded throughout the session (red), regardless of whether the units showed its largest waveform on two most dorsal recording sites (N = 42) or two most ventral recording sites (N = 19), suggesting that either these new fields did not emerge due to backpropagating action potentials, or the inability to capture such events with extracellular physiology. *(F)* The mean±SEM inter-spike interval histogram for remapping cells for spikes recorded in the location centered on the post-stimulation place field (green = pre-first pass with 3Hz; black = first trial in which firing was > 3Hz; red = all subsequent trials in which firing was > 3Hz). *Inset,* the proportion of spikes observed within a burst (<7ms ISI) for spike trains observed on the first place field pass, and all other place field passes in which the rate was > 3 Hz.

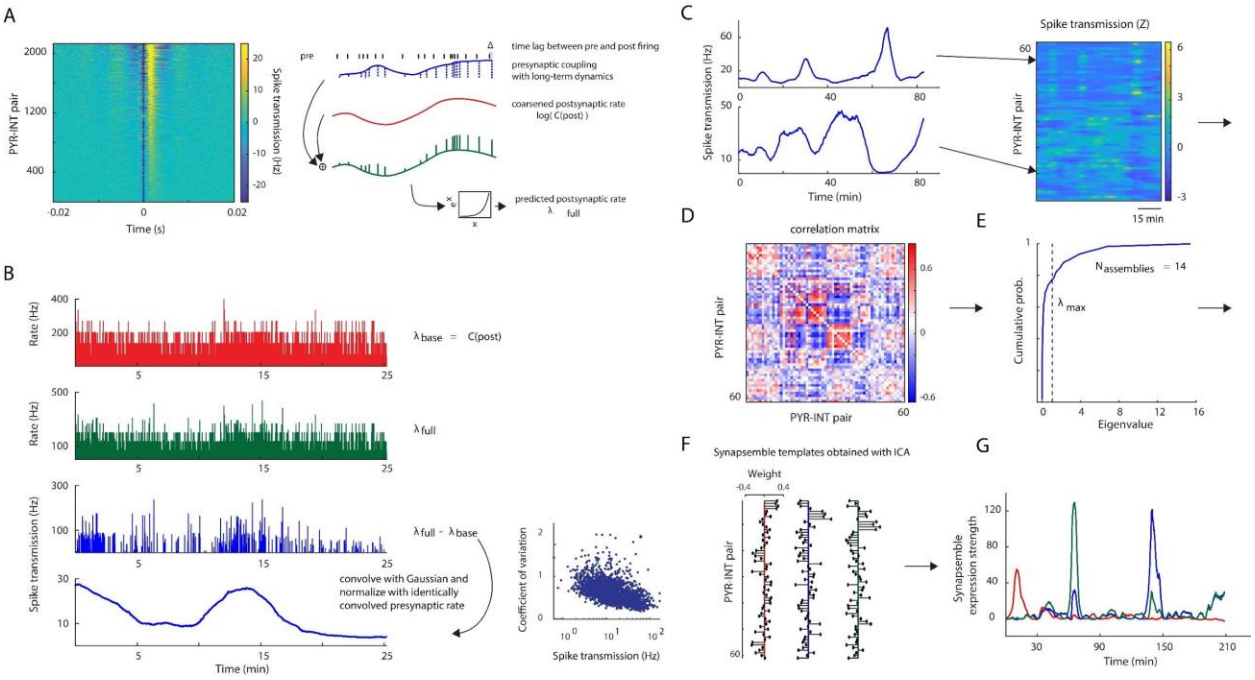

Figure S4. Calculation of time-resolved spike transmission and synapsemble detection; related to Figure 6. *(A) Left,* Monosynaptically connected pairs of pyramidal cells and interneurons (N = 2,132) were detected as described in English et al., 2017. Baseline corrected cross-correlograms (CCGs) of all PYR-INT pairs are ordered by spike transmission strength, defined as excess rate in the 0.8–2.8 ms bins above the baseline (English et al., 2017). *Right,* Schematic of a generalized linear model used to compute a time-resolved estimate of spike transmission. Before being passed through the spiking nonlinearity (green bottom trace), the postsynaptic rate of the interneuron is modeled as a linear combination of the log-transformed slow time varying (binned at 15ms and linearly interpolated) postsynaptic rate (red) and a time-varying rate-gain at the moment just after presynaptic spiking (blue). *(B) Left,* To estimate the time-resolved spike transmission between a PYR-INT pair, the coarsened postsynaptic rate (red, λ_{base}) was subtracted from the full model (green, λ_{full}) described in Panel A. This difference (blue, λ_{diff}) reflects the time-varying postsynaptic rate at monosynaptic latency after each presynaptic spike, over and above what can be expected from slow changes in the postsynaptic rate alone. In order to obtain a smooth estimate of this quantity in units of rate per presynaptic spike, λ_{diff} was convolved with a Gaussian (SD = 120 seconds) and divided by the presynaptic spike train convolved in the same manner. Note, the high values on the y-axis reflect expected spike counts per 0.8 ms time bins expressed as rates (spikes/sec). *Right,* The magnitude of fluctuations in spike transmission was quantified using the coefficient of variation (CV = 0.647 ± 0.005). *(C) Left,* Spike transmission time series of two PYR-INT pairs (left) are shown in an example session (61 pairs). *Right,* The time series are downsampled to 10 Hz, z-scored, and represented as a matrix. *(D)* Correlation matrix of all pairs in this session. Positive off-diagonal values reflect pairs whose spike transmissions co-fluctuate. *(E)* PCA was applied to the correlation matrix, and the number of significant spike transmission coactivation patterns ('synapsembles') was estimated as the number of eigenvalues exceeding the analytical threshold λ_{max} based on the Marcenko-Pastur distribution. *(F)* Z-scored data (as shown in Panel C) was projected onto the subspace of PCs whose eigenvalues exceeded λ_{max}, and ICA was used to identify synapsemble templates. Example

synapsembles are represented as a whisker plot. *(G)* Time-resolved expression strengths of the 3 synapsembles shown in Panel F. The synapsemble expression strength is defined as the bin-by-bin squared projection of the z-scored excess synchronies onto a given synapsemble template (see STAR Methods).

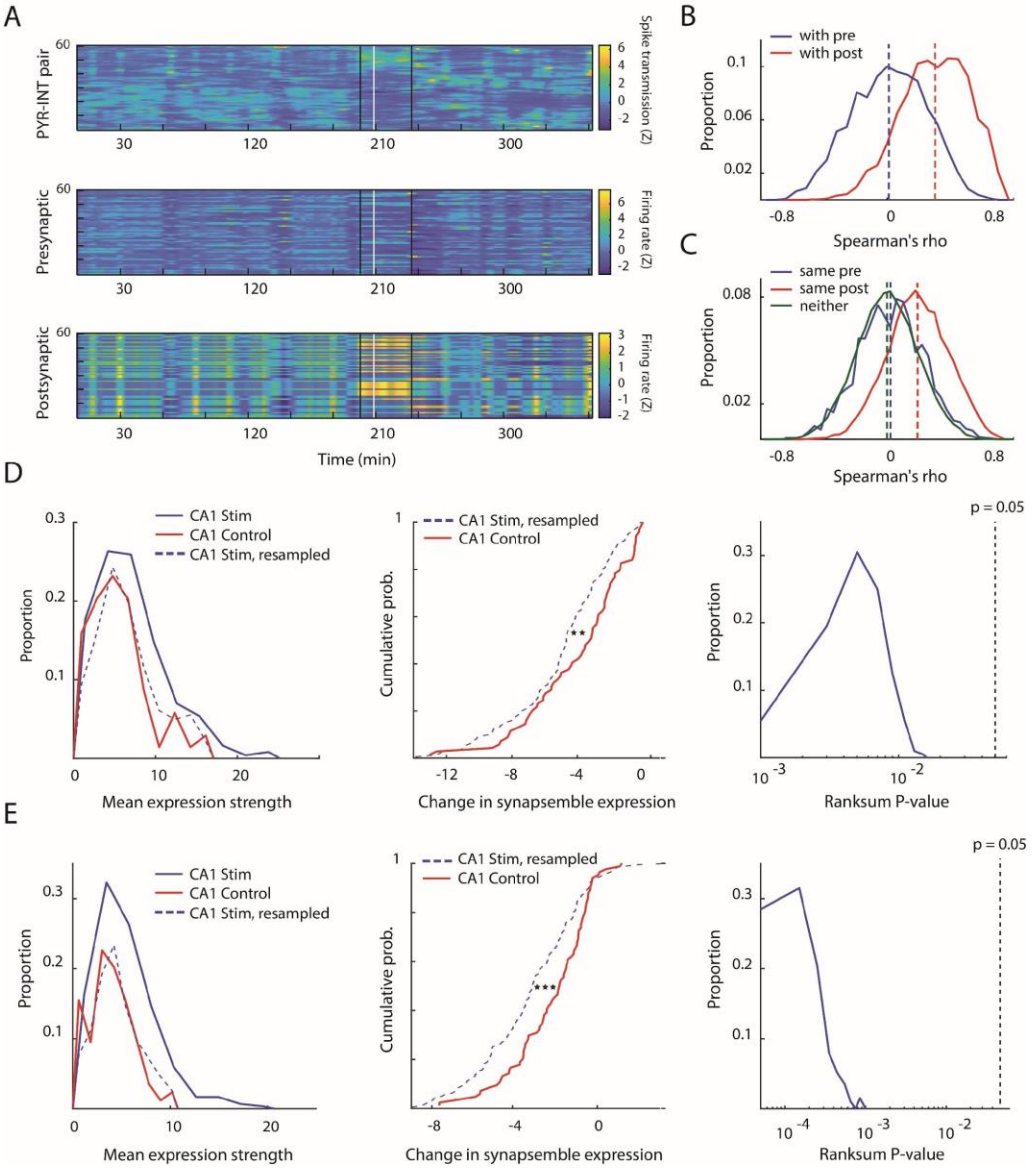

Figure S5. Spike transmission is not fully accounted for by rate, and synapsemble rearrangements are robust with respect to differences in baseline expression; related to Figure 6. *(A) Top* Spike transmission time series in a session different from that shown in Figure B. *Middle* Z-scored firing rates of the presynaptic pyramidal cells (ordered according to pair membership above). Spikes were convolved in the same way as the baseline corrected spike transmission time series (λ_{diff}, see STAR Methods). *Bottom*, Same as middle, but for postsynaptic interneurons. *(B)* Distributions of Spearman correlation coefficients between all presynaptic PYR rates (blue, N = 1,771, R = 0.0124) and spike transmission time series of the pairs they belong to and between postsynaptic INT rates (red, N = 1,771, R = 0.38) and the spike transmission time series of the pairs they belong to. Note that firing rate fluctuations of the presynaptic pyramidal neurons do not (on average) affect the spike transmission measure. *(C)* Spearman correlation

coefficient distribution among excess synchrony time series sharing a presynaptic PYR (blue, N = 1,977, R = 0.027), a postsynaptic INT (red, N = 12,581, R = 0.24), or sharing neither (green, N = 42,859, R = 0.0003). *(D) Left,* Distributions of mean synapsemble expression strengths during Pre-stim recording (when synapsembles were detected) were different between CA1 stim (blue, N = 243) and control (red, N = 69) sessions ($p > 0.05$, Mann-Whitney U-test) samples. We considered that changes in synapsemble expressions (Figure 6F,G) could be a statistical artifact due to this difference in baseline. To control for this possibility, we sampled from the CA1 stim distribution according to the empirical cumulative distribution function of the CA1 control distribution. This yielded a surrogate CA1 stim distribution (blue dashed) that was no different from CA1 control ($p < 0.01$, Mann-Whitney U-test). *Middle,* Distributions of changes in mean synapsemble expression strengths between CA1 Control and resampled CA1 stim were significantly different ($p < 0.01$, Mann-Whitney U-test), supporting the result in Figure 6F. *Right,* The distribution of Mann-Whitney U-test p-values for N = 200 independently resampled CA1 stim distributions lies below the significance threshold ($p = 0.05$), suggesting that the results of this control analysis are robust with respect to the randomness of resampling. *(E)* Same as D), except synapsembles were detected during Post-stim recording.

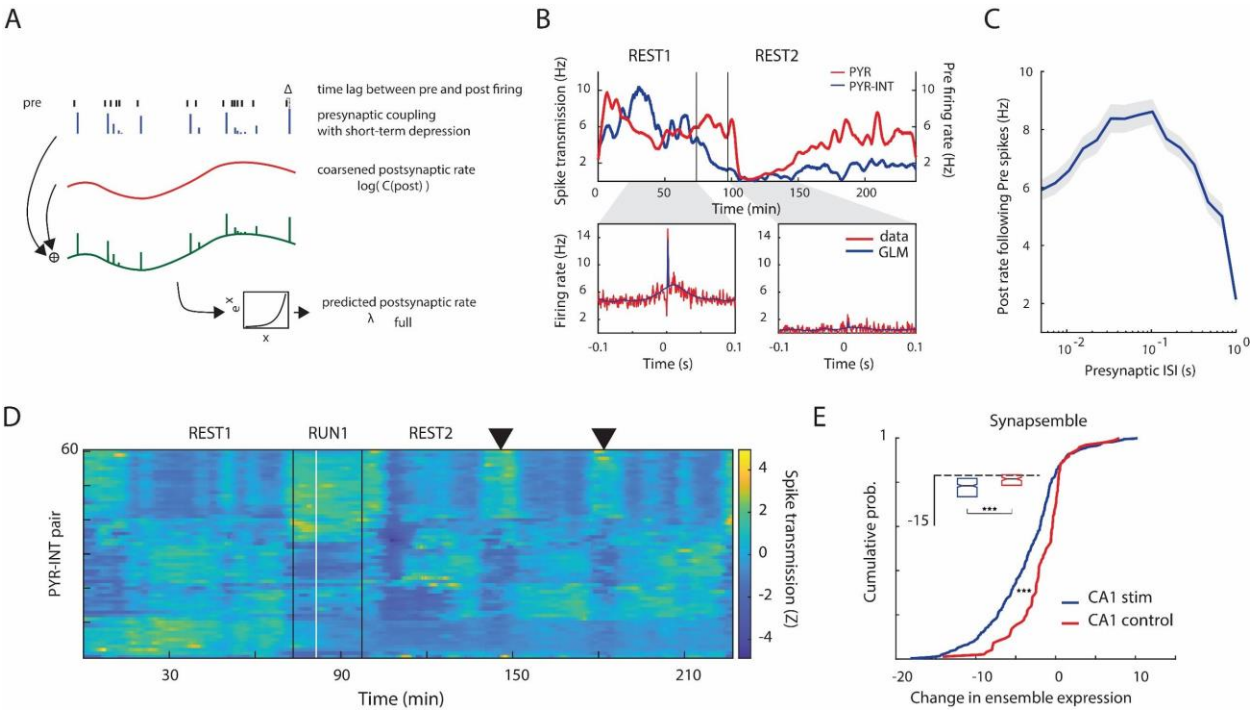

Figure S6: **Perturbation-induced PYR-INT rearrangement in an alternative model of spike transmission dynamics; related to Figure 6**. *(A)* Schematic of the extended GLM for capturing spike transmission dynamics fluctuating according to the Tsodyks-Markram model for short-term plasticity. In the case of short-term depression, coupling strength is greatest following long presynaptic ISIs (as visualized), while for short-term facilitation, coupling strength grows following short presynaptic ISIs. *(B) Top*, Spike transmission (blue) between a PYR-INT pair for which a full short-term plasticity model provided the best fit, and the presynaptic firing rate (red) to illustrate the nontrivial relationship between presynaptic firing and spike transmission. *Bottom*, Observed and GLM-predicted cross-correlograms for the example PYR-INT pair, calculated in 50-minute time periods in the homecage prior to and following track running. *(C)* Mean GLM-predicted postsynaptic firing rate (SEM) as a function of presynaptic ISI. Presynaptic spikes were binned according to preceding ISIs, and the mean expected postsynaptic rate across bins at time lags with respect to these spikes was computed. *(D)* Z-scored spike transmission time series between 61 PYR-INT pairs in a single session. ▼ highlights a recurring synapsemble, as in Figure 6B. *(E)* Stimulation induced larger changes in synapsemble expression (blue, N = 450) than in Control sessions (red, N = 151; $p < 0.001$; Mann-Whitney U-test), as in main Figure 6F.